1 **THE ROLE OF POROSITY IN EXTERNAL SULPHATE ATTACK**
2
3 Tai Ikumi[a],*, Sergio H. P. Cavalaro[b] and Ignacio Segura[a, c]
4
5 [a] Department of Civil and Environmental Engineering, Universitat Politècnica de
6 Catalunya, Barcelona Tech, Jordi Girona 1-3, C1, E-08034 Barcelona, Spain
7 [b] School of Architecture, Building and Civil Engineering, Loughborough University,
8 Leicestershire, LE11 3TU, United Kingdom
9 [c] Smart Engineering, Jordi Girona 1-3 K2M 202c, Barcelona, Spain
10
11 * Corresponding author: Tai Ikumi. Department of Civil and Environmental
12 Engineering, Universitat Politècnica de Catalunya Barcelona Tech, Jordi Girona 1-3,
13 C1, E-08034 Barcelona, Spain. Email address: tai.ikumi@upc.edu, Tel: +34 93 401
14 6507 Fax: +34 93 401 1036
15
16 **ABSTRACT**
17
18 Design codes promote a limitation of permeability (indirectly of porosity) to reduce the
19 sulphate ingress and improve the resistance of concrete and mortar to external sulphate
20 attack (ESA). However, porosity could also have a positive effect on durability by
21 generating additional space to accommodate the expansive phases. The aim of this study
22 is to evaluate the role of porosity in ESA. For that, changes at the macro-scale, phase
23 composition and pore network are monitored for mortar compositions with different
24 pore-size distribution. Results indicate the existence of two mechanisms: the capacity to
25 accommodate expansive phases controls the durability during the initial stages of the
26 attack, while at later stages durability is defined by the permeability. Results from
27 specimens with air-entrainer suggest that the intentional increase of porosity towards
28 maximising the capacity to accommodate expansive products might be a valid approach
29 in order to reduce the expansive forces generated during ESA.
30
31 **Keywords:** Sulphate Attack (C), Ettringite (D), X-Ray Diffraction (B), Mercury
32 Porosimetry (B), Pore structure
33
34 **1. INTRODUCTION**
35
36 External sulphate attack (ESA) is a complex degradation process that can compromise
37 the long-term durability of cement-based materials in contact with sulphate-rich
38 environments. ESA requires the penetration of sulphate ions from an external source
39 into the cementitious material. The connection between the external aqueous media and
40 the pore solution alter the equilibrium conditions in the liquid system, leading to a net
41 mass flow and subsequent chemical reactions to restore a minimum energy state. The
42 chemical reactions triggered define the damage mechanism associated with the attack.
43 ESA caused by sodium sulphate is characterised by ettringite and gypsum formation in
44 such a quantity that the material sustains chemical and physical damage. Chemical
45 damage refers to the degradation of mechanical properties in the cementitious matrix
46 caused by the decalcification of hydrated phases, while physical damage is usually
47 related to the degradation caused by expansive forces generated at the pore-level. These
48 forces are ultimately responsible for the development of expansions and possible
49 cracking and spalling [1,2].
50

There is still controversy on how ettringite and gypsum formation are converted into actual expansions. The prevailing theories are the volume increase approach and the crystallisation pressure theory. The first assumes that the expansions observed are the result of the additional volume generated by the expansive products precipitated during the attack (e.g. [3]). Therefore, the amount of ettringite precipitated determines the magnitude of the expansions. The latter states that expansions are caused by the crystallisation pressure exerted on the pore walls due to the formation of ettringite [4,5]. In this case, ettringite has to be growing from a supersaturated solution in confined conditions in order to convert the chemical energy into mechanical work, meaning that not all ettringite contributes to the expansions. Recent investigations place the crystallisation pressure theory as the most plausible, with it currently the most accepted mechanism of damage [6]. A comprehensive review of the main suggested theories can be found in [2].

Building and structural codes specify precautionary measures when obtaining sulphate-resisting concrete. These measures consist of limiting the aluminate content in the cement, using low water/cement ratios to reduce the permeability and increasing of compressive strengths to resist the internal stress caused by the expansion (e.g. Model Code 2010, BS 8500-1:2006, ACI 201.2R-08, UNE EN 206-1:2008). The recommendation of low permeability seeks to reduce the penetration of external aggressive ions into the inner layers of the material, with several studies supporting such a recommendation. Nowadays, it is accepted that cement-based materials with low permeability show a better durability against sulphates than the corresponding samples with higher permeability (e.g. [1,2,7-10]). Although permeability and porosity are not synonyms, in general the fall-off in permeability is accompanied by a consequent decrease in the porosity of the matrix. Therefore, the limitation of permeability usually indirectly implies a reduction of the porosity provided by the pore network.

However, the role of the pore network during the attack is not only related to the transport of sulphate ions. Since pores are basically empty spaces within a rigid matrix, they have a certain capacity to accommodate expansive phases before creating damage. In this context, pores might act as deposits or containers of the expansive products precipitated during ESA. This phenomenon has been described by other authors [3,11-13] as the buffer capacity of the matrix and it is directly or indirectly considered in both damage mechanisms previously mentioned.

Some studies report trends that may suggest the positive consequence of a highly porous material in comparison with a dense matrix with low permeability and porosity. Naik et al. [14] found that a reduction of the water/cement ratio caused more severe physical damage in samples exposed to a sodium sulphate solution. The authors attributed the earlier damage and the more rapid failure of the samples to the reduced extensibility of the material and the low capacity of the dense pore network to accommodate expansive phases [14]. M. Santhanam et al. [15,16] assessed the behaviour of mortars with a presumably high capacity to accommodate expansive phases by the use of an air-entrainer admixture. The authors obtained delayed levels of deterioration in such mortars, suggesting that entrained air might provide sites for nucleation of expansive phases, which might in turn lead to a reduced damage in the paste. Another hypothesis formulated was that air might help arresting the growth of cracks due to their spherical shape.

101 Despite that, solid evidence and explanations regarding the contribution of a highly
102 porous matrix are rare and inconclusive. Consequently, the maximisation of the buffer
103 capacity of the matrix by increasing the porosity has not been recognised as a possible
104 approach to obtain more durable materials against ESA.
105
106 The objective of this study is to assess the influence of the pore network on the
107 durability against ESA. For that, mortar compositions with different porosities (from
108 8.1 % to 18.8 %) are subjected to accelerated sulphate attack. In order to isolate the
109 effects of porosity, C_3A content, external sulphate concentration and geometrical
110 characteristics of samples are kept constant for all compositions. Characterisation of the
111 macro-scale behaviour is performed by monitoring the dimensional, mass and ultrasonic
112 velocity variation over time. Changes in phase composition are investigated by X-ray
113 diffraction (XRD) and evolution of the pore characteristics of the mortars are examined
114 by mercury intrusion porosimetry (MIP).
115
116 This study provides evidences and explanations that help understanding the role of
117 porosity in samples subjected to ESA. The findings might open up alternative strategies
118 for the future design of durable cementitious materials against the attack.
119
120 **2. EXPERIMENTAL PROGRAMME**
121
122 2.1 MATERIALS AND MORTAR COMPOSITIONS
123
124 Portland cement (CEM I 52.5R) with high C_3A content was used in order to promote
125 ettringite formation and the potential damage during ESA. Table 1 shows the chemical
126 (determined by XRF spectrometry) and mineralogical (estimated using Bogue
127 equations) composition and summarises the physical properties of the cement. Data
128 provided by Bogue equations is only used to classify the cement as highly reactive
129 under sulphate exposure. De-ionised water and siliceous sand following the
130 specifications of UNE-EN 196-1:2005 were used in all mortars. Commercial
131 superplasticiser GLENIUM ACE 456 and air-entrainer MasterAir 100 were added to the
132 mixtures.
133
134 Table 1. Chemical and mineralogical composition of the Portland cement.

Chemical composition [% bcw*]	
SiO_2	19.5
Al_2O_3	5.9
Fe_2O_3	1.7
CaO	63.1
MgO	2.1
SO_3	3.5
K_2O	0.8
Na_2O	0.4
Cl^-	-
LOI	3.0
Phase composition [% bcw*]	
C_3S	65.4
C_2S	10.6
C_3A	12.3
C_4AF	5.6
Physical properties	
Spec. surf. area (BET) [m^2/g]	1.10

d_{10} [µm]	0.58
d_{50} [µm]	6.88
d_{90} [µm]	31.84

bcw: by cement weight

Table 2 shows the composition of the four matrices included in this study. Different degrees of refinement of the pore network were obtained by varying the water/cement ratio from 0.38 to 0.55 and by using an air-entrainer. Initial reference porosities obtained by MIP test at 14 days after sulphate exposure are included in Table 2. The different compositions considered cover a wide range of porosities (from 8.1 % to 18.8 %). The nomenclature adopted for each composition follows the pattern *water/cement ratio – initial porosity*. Air-entrained mortars have the term '*AE*' prior to the water/cement ratio. Notice that the cement content remained constant for all compositions, ensuring similar amount of C_3A and potential expansion. Therefore, the macro-scale response of mortars after sulphate exposure can be associated mainly to differences in the pore system.

The mixing procedure defined in UNE-EN 196-1:2005 was adopted, introducing small modifications to cover the specificities of the admixtures added. The air-entrainer was added at the end of the mixing procedure and mixed at high speed for 60 seconds. The superplasticiser was mixed with the de-ionised water in contents to assure flow extents of 20 cm ± 0.5 cm. This flow extent was defined to favour similar workability and surface finish amongst all mortar compositions.

Table 2. Compositions and mass attenuation coefficient (MAC) of the mortars.

| Material	0.38_8.1%	0.45_12.4%	0.55_13.7%	AE0.45__18.8%
Cement [kg/m^3]	580	580	580	580
Sand [kg/m^3]	1425	1325	1180	1325
Water [kg/m^3]	220	261	319	261
Air-entrainer [% bcw]	-	-	-	0.3
Superplasticiser [% bcw]	1.00	0.50	-	0.25
Water/cement ratio	0.38	0.45	0.55	0.45
Porosity [%]	8.1	12.4	13.7	18.8
MAC [cm^2/g]	48.11	48.01	47.84	48.01

2.2 EXPERIMENTAL PROCEDURE

2.2.1 SPECIMEN PREPARATION

Ø78 mm x 17 mm mortar specimens were cast to conduct this study. Such geometry was chosen to avoid the typical corner spalling observed in rectangular samples that might alter the macro-scale response during the attack [17]. The dimensions selected maintain similar exposed surface-volume ratio than other studies that showed good balance between test duration and representativeness [18]. Due to the importance of the surface finish in transport-related degradation processes, specimens were cast in individual moulds to obtain external surfaces representative of field conditions and to avoid the presence of cut aggregates on the exposed surfaces.

Figure 1 shows a schematic representation of the moulds and the casting process adopted. The moulds comprised a PE rigid base with four fixed PVC pipes and a movable PE rigid cover. Top and side views of these components are shown in Figure 1a. Five Ø12 mm x

175 160 mm bolts were used to guide the cover into the base during assembly (Figure 1b),
176 while twelve PE bars were used to fix the PVC pipes and block the cover at a specific
177 height to obtain a sample thickness of 17 mm. To relieve the excess mortar, purge exits
178 were introduced in the cover. Before assemblage, the mortar (represented in light hatching)
179 was first poured inside the PVC pipes and compacted with 15 jolts in the flow table
180 (ASTM C1437) at a rate of one jolt per second to eliminate air pockets. After that, the
181 cover was placed and tightened to the base. In order to ensure adequate surface finish
182 quality, the moulds were then vibrated for ten seconds at the vibration table. Finally, the
183 hex nuts were further tightened until the cover reached the PE bumpers that control the
184 height of the specimens.
185
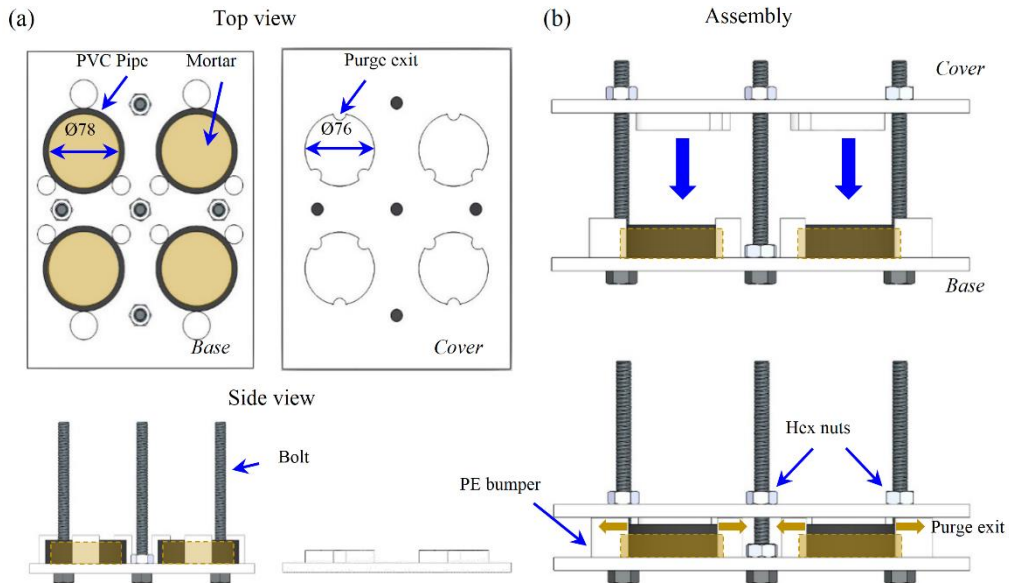
186
187
188 Specimens were demoulded 24 hours after casting and the lateral surface was water-
189 sealed with MasterSeal M 338 flexible epoxy coating to ensure linear penetration of the
190 sulphate ions through the two main surfaces of the specimen. Figure 2a shows a final
191 specimen obtained after applying the coating. Once sealed, all specimens were cured in
192 water at 25 ℃ ± 1 ℃ for 24 hours. Then, they were placed laterally inside plastic
193 containers and submerged in a sulphate-rich water solution (Figure 2b).
194
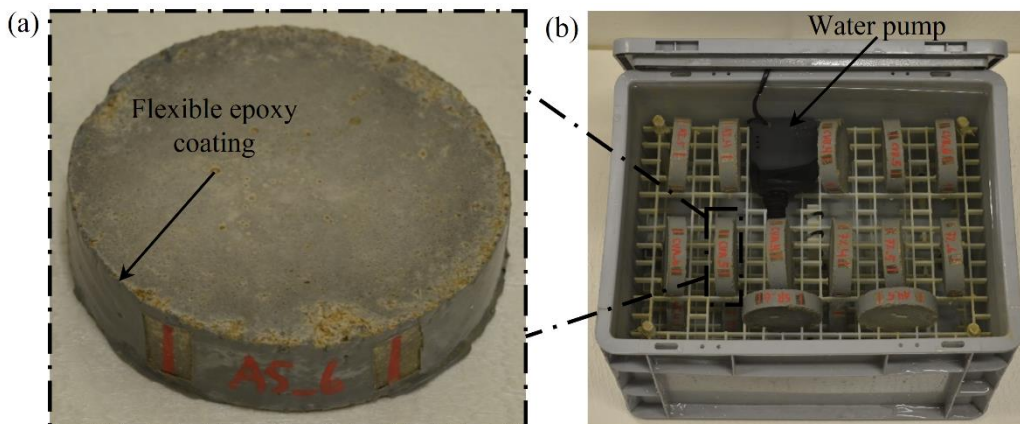
195
196
197 2.2.2 EXPOSURE CONDITIONS
198

199 Specimens were exposed to the sulphate solution shortly after casting to reproduce the
200 real exposure conditions of most structures subjected to ESA, which are usually built *in*
201 *situ*. Sulphate concentration of 30 g of Na_2SO_4/l was used to accelerate the degradation
202 process [19]. The solution was renewed weekly during the first month and every other
203 week until the end of the test at 365 days. The volumetric ratio of sulphate solution to
204 mortar was 12, a level that should be representative of field conditions where the
205 material is exposed to continual supply of sulphate ions.
206
207 Water pumps were placed inside the plastic containers to ensure a continuous flow from
208 the bottom to the top in order to minimise concentration gradients (Figure 2b). The
209 containers were filled to the top and covered to reduce contact with the air, thus limiting
210 CO_2 dissolution and carbonation. Reference samples of each composition were also
211 exposed to non-aggressive curing with water without sulphates for comparative
212 purposes.
213
214 2.2.3 TEST METHODS
215
216 - *Macro-structural monitoring*
217
218 Characterisation of the macro-scale behaviour relies upon measurements of expansion,
219 mass and ultrasonic velocity and visual inspection of the specimens. All measurements
220 were taken weekly during the first month and every other week until the end of the
221 study. The values presented in this study are the average of three specimens.
222
223 Due to the singular shape of the specimens, a device was designed to measure the radial
224 free expansions of the mortars (Figure 3a), which consisted of a MICROMASTER
225 electronic micrometer with a precision of ± 0.001 mm and a metallic platform to fix the
226 measured points. Several vertical strips were introduced to facilitate the measuring and
227 to guarantee a similar position of the specimens (Figure 2a). Prior to the start of the
228 experimental programme, the precision of the equipment was evaluated during a series
229 of over 500 measurements on mortar specimens with and without gauge studs.
230 Specimens with gauge studs obtained higher variability of the measurements (± 0.008
231 mm with studs and ± 0.002 mm without studs). Consequently, the use of studs was
232 discarded. For each specimen, three radial directions were measured at each time to
233 cover all the sample (Figure 3b). Therefore, each expansion value presented in this
234 study is the average of nine measurements.
235
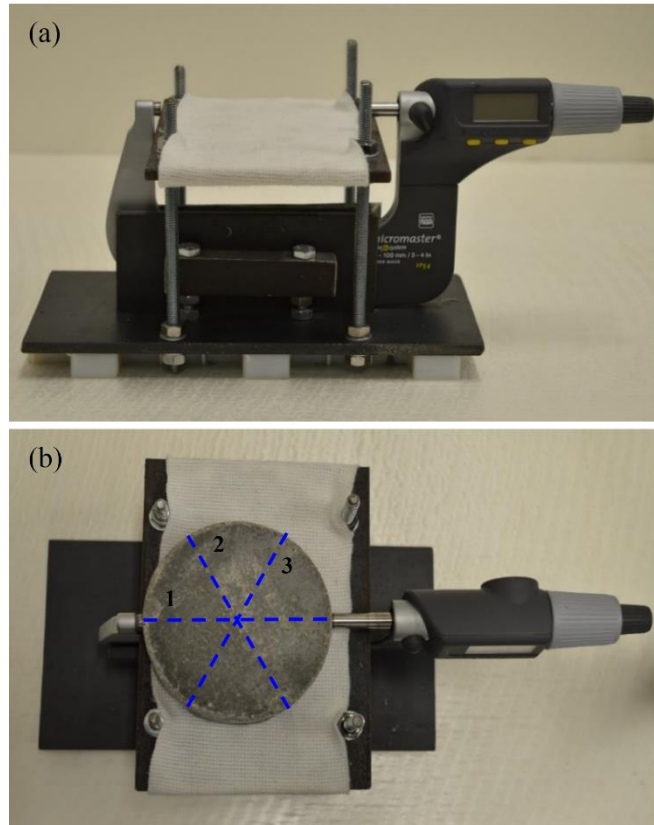
(a)

(b)

236
237
238 The ultrasonic pulse velocity between the two exposed faces was measured at 500 kHz
239 sampling frequency using a PUNDIT PL-200, while a zero-crossing algorithm was used
240 to calculate the travelling time of the ultrasonic wave. Mass evolution was controlled
241 with a precision balance of ±0.01 g. Surface water of the samples was dried up before
242 weighting.

243

244 - *Phase composition evolution*

245

246 Changes in phase composition were examined using X-ray diffraction (XRD) at 28, 90,
247 180, 270 and 365 days. Samples for XRD were core-drilled from original specimens
248 using a column drill equipped with a water-cooled diamond drill bit [20]. For each
249 composition, samples were extracted from the same specimens to reduce the variability
250 of the results. Due to the symmetric sulphate exposure conditions, each sample was
251 divided in two. One half was crushed and the powder was pressed in cylindrical
252 standard sample holders of 16 mm diameter and 2.5 mm height, while the other half was
253 discarded. XRD measurements were made using a PANalytical X'Pert PRO MPD
254 Alpha1 $\Theta/2\Theta$ diffractometer in reflection Bragg Brentano geometry of 240 mm of
255 radius. CuK$_{\alpha 1}$ radiation (λ=1.5406 Å) and X'Celerator detector with active length of
256 2.122 ° were used. Work power was set to 45 kV – 40 mA. $\Theta/2\Theta$ scans from 4 to 80 º2Θ
257 with a step size of 0.017 º2Θ and a measuring time of 50 seconds per step were
258 performed. Sample holders were spun at two revolutions per second.

259

260 Rietveld analysis using the external standard method was performed on the XRD results
261 for the quantitative study of the crystalline phases. The external standard method was
262 used for quantification instead of the more common internal standard method to avoid
263 homogenisation problems and further dilution of the cement paste in the analysed

264   sample [21-23]. The adopted methodology is similar to earlier works [21-23]. Phase
265   weight fractions were calculated from phase scale factors by comparison to the scale
266   factor of the external standard (Al_2O_3), measured under identical diffractometer
267   conditions. The density and volume values of the unit cell of each phase were obtained
268   from data sets from ICSD. Mass attenuation coefficients (MAC) of the different
269   compositions used were calculated from the MAC of each component, including the
270   water content and taking into account the weight fraction of each one. Final MAC of the
271   different mortars used are listed in Table 2.
272
273   All Rietveld refinements were carried out with X'Pert High Score Plus software
274   package by PANalytical, using the structures listed in Table 3. Small peaks of Fe-
275   substituted ettringite formed as a result of the reaction between sulphate ions and the
276   ferroaluminate phases were detected in some mortars at late stages of the attack. Since
277   its crystalline structure for Rietveld refinement was not available it was not considered
278   during quantification. The global variables refined were the background polynomial
279   with 4 coefficients (1st, 2nd, 3rd and 5th) and the zero shift. For all phases detected,
280   individual scale factors and lattice parameters were refined. A pseudo-Voigt function
281   was chosen to model the peak shape. The phase profile width (w) was refined for quartz,
282   ettringite, portlandite and gypsum. For quartz and portlandite, the profile parameters U,
283   V and the peak shape were also refined. Preferred orientation corrections were applied
284   when necessary for gypsum (0 2 0), portlandite (0 0 1), ettringite (1 0 0) and quartz (1 0
285   1) as long as the phase content was above 2%.
286
287   Table 3. Phase structures used for Rietveld refinement.

Phase	Chemical composition	ICSD Code	Reference
Alite	Ca_3SiO_5	94742	[24]
Belite_o	Ca_2SiO_4	81097	[25]
Portlandite	$Ca(OH)_2$	15471	[26]
Calcite	$CaCO_3$	79673	[27]
Ettringite	$Ca_6Al_2(SO_4)_3(OH)_{12}26H_2O$	155395	[28]
Gypsum	$CaSO_42H_2O$	15982	[29]
Ferrite	Ca_2AlFeO_5	9197	[30]
Quartz	SiO_2	200721	[31]
Corundum	Al_2O_3	73725	[32]

288
289   *- Pore system evolution*
290
291   Evolution of the pore system of the mortars were examined through mercury intrusion
292   porosimetry (MIP) with a Micrometrics AutoPore IV 9500 (contact angle 140º and Hg
293   surface tension 485 dynes/cm) at 14, 28, 91, 180 and 270 days. Tests after 270 days
294   were not performed due to the spalling of the external layer of the sample during
295   drilling. Samples were extracted following the same procedure as described in the
296   previous section. Due to the symmetric sulphate exposure conditions, each sample was
297   divided in two halves and analyzed separately, before the samples were freeze-dried to
298   ensure full desaturation prior to mercury intrusion.
299
300   **3. RESULTS AND DISCUSSION**
301
302   3.1 MACRO-STRUCTURAL CHARACTERISATION
303

304   3.1.1 VISUAL APPEARANCE OF SAMPLES
305
306   Visual appearance during the attack indicates no major failure in any composition in the
307   form of generalised spalling of the external surface or tensile splitting of the sample.
308   The geometrical characteristics and specimen preparation adopted in this study
309   prevented the development of failure modes that might compromise the interpretation of
310   the macro-structural response of the material.
311
312   Figure 4 depicts the visual appearance of the external surface of the four compositions
313   at the end of the test. In 0.38_8.1%, 0.45_12.4% and 0.55_13.7%, a thin, dense layer
314   covering most of the surface was observed. This layer appeared in small localised
315   regions approximately in the second month of exposure and spread at different rates
316   until the end of the test. Samples with lower water/cement ratio (0.38_8.1% and
317   0.45_12.4%) showed the higher formation rates. As a result, these samples experienced
318   localised spalling in locations within the region covered by the layer. In Figure 4, these
319   locations are highlighted with a red circle.
320
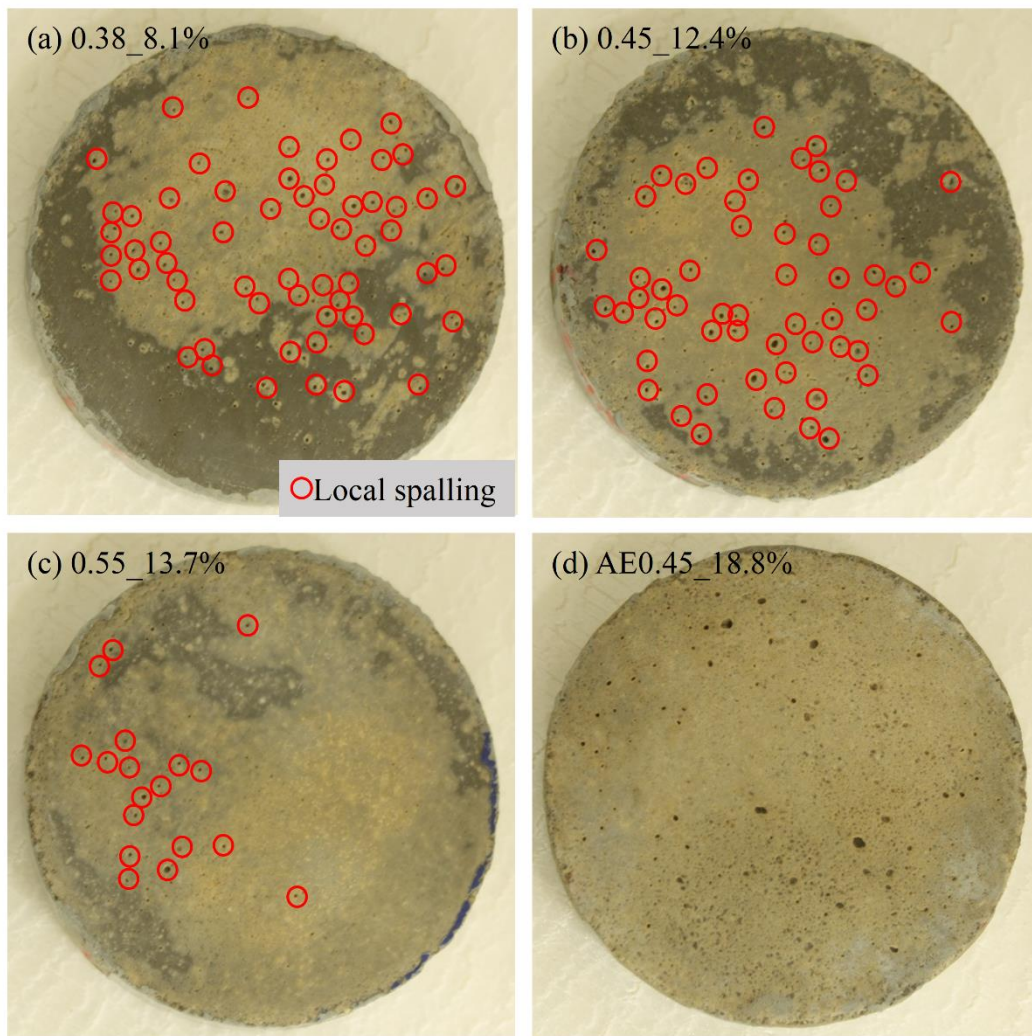
321
322
323   A comparison of the amount of red circles between Figure 4a, 4b and 4c clearly
324   indicates that the physical damage in the form of local spalling increases with the
325   decrease of the porosity of the samples. This observation concurs with the results

326   presented by Naik et al. [14]. On the other hand, in mortars with air entrained (Figure
327   4d) this dense layer is not visible at any stage of the attack.
328
329   3.1.2 EXPANSIONS
330
331   Figure 5 depicts the radial expansion of the mortars during the 365 days of sulphate
332   exposure. In order to distinguish the effects of sulphate exposure from the normal
333   hydration process, data presented in Figure 5 corresponds to the difference between
334   exposed and control specimens. Due to the large number of measuring points at each
335   curve, +1/-1 standard deviation bars are only depicted at 28, 90, 180, 270 and 365 days.
336   The maximum, minimum and mean standard deviation of all radial expansion
337   measurements are $1.28 \cdot 10^{-4}$, $2.36 \cdot 10^{-5}$ and $5.71 \cdot 10^{-5}$ respectively. Results for
338   0.38_8.1%, 0.45_12.4% and 0.55_13.7% series show a first stage of rapid expansions
339   followed by a second stage characterised by a decrease in the expansion rate. In the case
340   of 0.55_13.7%, this decrease is considerably less pronounced than in the other
341   compositions. The duration of the first stage is approximately 77, 63 and 25 days
342   respectively for 0.38_8.1%, 0.45_12.4% and 0.55_13.7%, as indicated by the vertical
343   lines on each expansion curve (duration estimated by the first consecutive measure
344   where the expansion increase is below 5%).
345
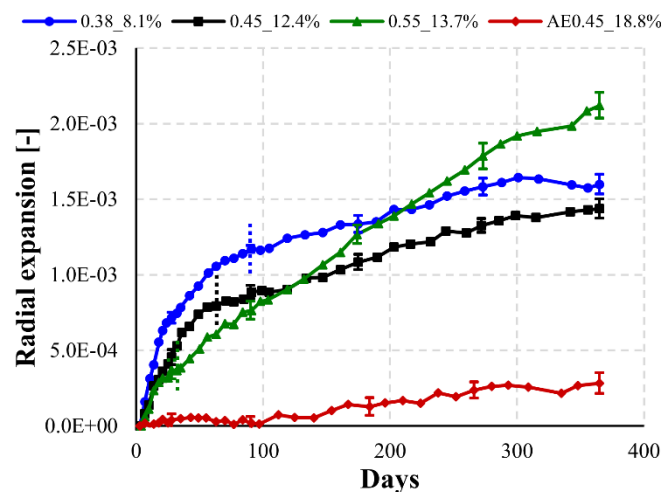
346
347
348   The first stage may be caused by the high initial sulphate concentration gradient
349   between the solution outside and inside the specimen. Moreover, the early exposure
350   facilitates sulphate ingress due to the low densification of the matrix at this moment.
351   Therefore, a sudden sulphate concentration boost in the pore solution of the matrix close
352   to the surface should be observed. This may cause ettringite precipitation and
353   crystallisation pressure increase at locations where calcium, aluminium and sulphates
354   meet. According to the prescriptions included in codes, the magnitude of the expansions
355   should be more evident in the compositions with higher porosity, as the penetration is
356   presumably enhanced. However, Figure 5 shows the opposite trend for the first stage of
357   the expansion curve, as mortar 0.38_8.1% presents the highest expansions but the
358   lowest porosity.
359
360   This behaviour might be explained by a retardation of the cement hydration derived
361   from the different dosages of superplasticiser adopted in the compositions. This may
362   lead to higher initial porosities in the matrices with higher dosages (0.38_8.1%), prior to

363 the first porosity measurement performed at 14 days. Even though this hypothesis is in
364 line with the established knowledge on ESA included in codes, it presents several
365 shortcomings. First, the effects on cement hydration from polycarboxylate
366 superplasticisers are usually reported to alter up to 3 days of hydration [33]. Since the
367 mortars were exposed to the sulphate solution 48h after casting, the effects of the
368 superplasticiser on the pore structure should be minor. Moreover, it seems unlikely that
369 these effects overcome the large difference on water contents introduced by the different
370 water/cement ratios adopted. Finally, the trends described are consistent after the first
371 porosity measurement (at 14 days of exposure), where it is confirmed that the decrease
372 of water/cement ratio leads to a reduction of porosity.

374 Alternatively, it is believed that in this stage expansions are defined by the capacity of
375 the matrix to accommodate expansive products. In refined pore networks, the initial
376 sulphate concentration boost might cause sudden ettringite precipitation in small pores,
377 as the dense matrix force the sulphate flux through small capillary pores before reaching
378 larger pores. Due to the large availability of large pores in coarse pore networks, the
379 precipitation could mainly occur in locations with a high capacity to accommodate
380 expansive phases without creating expansion [15,16].

382 The decrease of expansion rates observed in the second stage for series 0.38_8.1%,
383 0.45_12.4% and 0.55_13.7% might be related to the kinetics of diffusion (reduction of
384 concentration gradient) and the influence of a pore-filling effect in the diffusion
385 coefficient of the external layers of the samples. Interestingly, the reduction of the
386 expansion rate is also related to the porosity of the mortars. In this case, mortars with
387 lower porosity (0.38_8.1% and 0.45_12.4%) show bigger reductions in the expansion
388 rate in comparison with mortars with higher porosity (0.55_13.7%), which present
389 lower decrease. A possible explanation is that in refined pore systems, the precipitation
390 produced during the first stage severely hinders sulphate penetration later, thus
391 decreasing the expansion rates. In porous matrices, the precipitation achieved is not
392 enough to fill a significant fraction of the capillary pores. Consequently, the penetration
393 rate should not be significantly altered and expansions would only be slightly reduced.
394 This hypothesis explains the steady expansion of samples 0.55_13.7%.

396 The air-entrained mortar presents a particular evolution over time. For this series, no
397 initial expansion is observed in the first stage, its onset only occurring after 100 days of
398 exposure. However, the expansion rates observed are still smaller than in other
399 compositions. The absence of expansions during the first 100 days could be related to
400 the high capacity of the matrix to accommodate expansive product. Due to the extensive
401 availability of large pores relative to the amount of ettringite formed, the pore-filling
402 effect that hinders sulphate penetration described for the other compositions does not
403 apply. As a result, instead of a reduction of expansions in the late stages of the attack,
404 for this composition the expansion rate increased. In terms of the absolute values
405 reached at the end of the accelerated test, the total expansion of the composition with
406 air-entrainer is 7.5 times smaller than the composition with 0.55 water-cement ratio.

408 The profiles depicted in Figure 5 reflect the double role of porosity in ESA. To
409 highlight this, Figure 6 shows the incremental radial expansion at different periods of
410 exposure, with the error bars included in each column corresponding to a +1 standard
411 deviation. During the first 28 days, results indicate that the capacity of the matrix to
412 accommodate expansive product constitutes the main resistance mechanism against

413 ESA, as expansions decreases with the increment of porosity. However, from 90 days of
414 exposure this trend is reversed for the non-air-entrained mortars, as expansions decrease
415 with the decrease of porosity. Therefore, at this stage the permeability of the matrix is
416 the main factor that define the behaviour against the attack. Notice that the air-entrained
417 mortar shows the smallest increments of expansions in almost all periods evaluated.
418 This result may indicate that the first stage where the buffer capacity of the matrix
419 controls the overall resistance against the attack can be extended over time if a sufficient
420 amount of large pores are available.
421
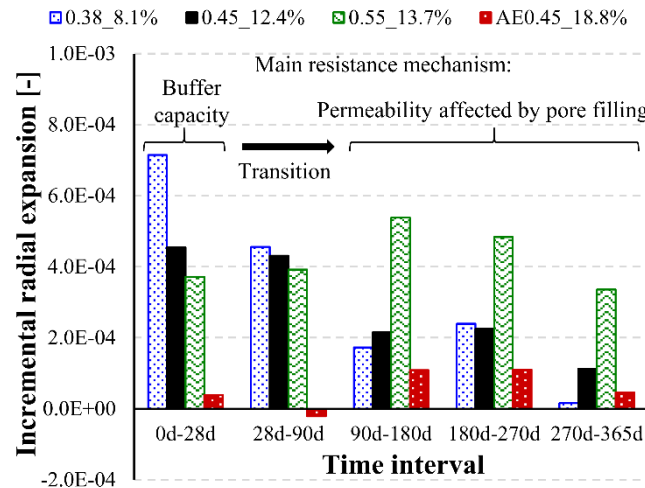
422
423
424 Figure 6 also sheds light on the reasons for the differences in behaviour found between
425 mixes 0.38_8.1% and 0.45_12.4%. The higher final expansion of the former is justified
426 by a significantly higher expansion in the period 0d-28d, which is approximately 57%
427 greater than the observed in 0.45_12.4% at the same period. In later periods, both
428 compositions show similar increments in radial expansion. Therefore, the bigger final
429 expansion of 0.38_8.1% in comparison with that from 0.45_12.4% is possibly the
430 consequence of a lower buffer capacity in the initial stages due to the more refined
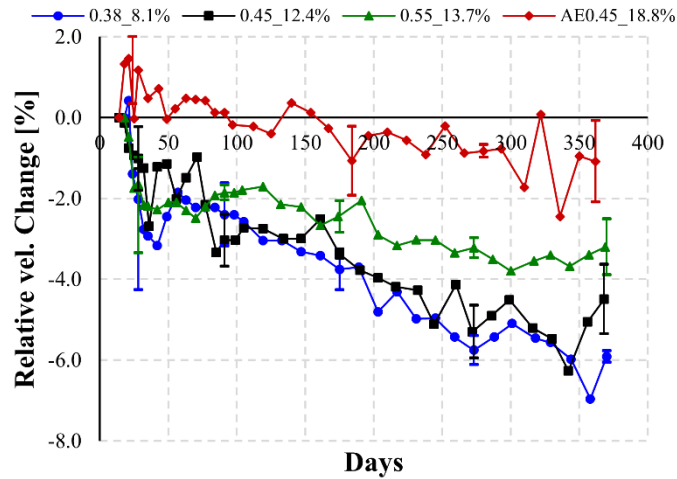431 porosity.
432
433 3.1.3 ULTRASONIC PULSE VELOCITY
434
435 Figure 7 shows the evolution of the ultrasonic pulse velocity for the different
436 compositions considered (difference between specimens stored in sulphate solution and
437 control at a certain time divided by the difference at the beginning of the accelerated
438 attack). Due to the large number of measuring points at each curve, +1/-1 standard
439 deviation bars are only depicted at 28, 90, 180, 270 and 365 days. The maximum,
440 minimum and mean standard deviation of all velocity change measurements are 2.35,
441 0.11 and 0.76 % respectively. Changes in velocity can be possibly related to the change
442 in the density and integrity of the specimens. Positive values suggest denser matrices
443 while negative values are indicative of damage. Samples from series 0.38_8.1%,
444 0.45_12.4% and 0.55_13.7% show similar trends with a decrease in ultrasonic velocity
445 with exposure time. As described in Figure 5 for the expansion, the relative velocity
446 change also depicts 2 stages. The first of these presents a rapid decrease of relative
447 velocity indicating high degradation rates. After that, a deceleration of the degradation
448 is observed, probably caused by the reduction of the penetration rate of sulphates due to
449 the pore-filling effect and the decrease of the sulphate concentration gradient, as

450 described in section 3.1.2. The differences observed amongst 0.38_8.1%, 0.45_12.4%
451 and 0.55_13.7% should be evaluated with caution, specially at early ages, as the
452 relatively high variability of the measurements might compromise analysis of the
453 results.
454

455
456
457
458 The evaluation of the velocity change at the end of the test shows that the degree of
459 damage increased in inverse proportion to porosity. In fact, the composition with the
460 denser matrix and smaller porosity (0.38_8.1%) presents the higher velocity reduction
461 amongst all the compositions studied, indicating relatively higher damage caused by the
462 attack. This result is in line with the visual inspection performed in section 3.1.1, but is
463 not consistent with the expansion profiles presented in 3.1.2 (at the end of the test,
464 0.38_8.1% did not show the highest dimensional variation). Such results could be
465 explained by the reduced extensibility of the material due to higher stiffness of the
466 denser matrix [14]. Therefore, even though a relatively higher damage occurs, the
467 higher elastic modulus restrains the deformation, leading to the assessment of lesser
468 expansion.
469
470 Air-entrained mortars (AE0.45_18.8%) meanwhile maintained similar velocities than
471 the control specimens throughout the accelerated attack, indicating low levels of
472 damage. These results are in line with the expansion curves presented in Figure 5, where
473 AE0.45_18.8% mortars exhibited the lowest expansions amongst all compositions.
474
475 3.1.4 MASS EVOLUTION
476
477 Figure 8 depicts the relative mass variation over time for all mortars studied. In order to
478 isolate the effects of sulphate exposure from the phenomena of absorption, hydration
479 and leaching experienced by all samples, this figure represents the differences between
480 exposed and control specimens. Due to the large number of measuring points at each
481 curve, +1/-1 standard deviation bars are only depicted at 28, 90, 180, 270 and 365 days.
482 The maximum, minimum and mean standard deviation of all relative mass change
483 measurements are 0.033, 0.003 and 0.011 % respectively. Notice that most error bars
484 are barely visible in the graph due to the low variability of the results. Despite the fact
485 that all samples presented a slight positive mass change, mortars subject to sulphate
486 exposure showed a much lower mass increase. Therefore, Figure 8 shows negative mass

487   variations for all compositions. Up to 200 days, sulphate exposure causes higher mass
488   reduction as porosity increases, while the mass of 0.38_8.1%, 0.45_12.4% and
489   AE0.45_18.8% mortars continues to decrease over time. However, 0.55_13.7% series
490   presents a change in tendency, showing a mass increase after 200 days.
491
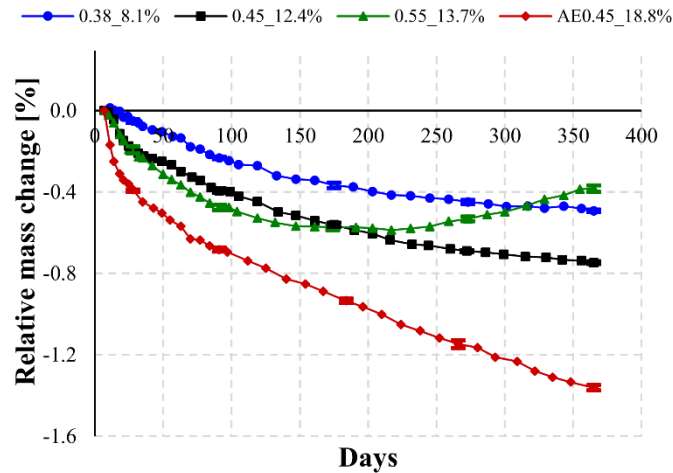
492
493
494   The mass reduction due to sulphate exposure could be explained by several processes
495   occurring after sample immersion. Mortars in the aggressive media experience sulphate
496   uptake from the external solution, which causes an increment of mass. However,
497   sulphate ingress triggers a series of chemical reactions that involves dissolution of
498   soluble calcium bearing phases for ettringite and gypsum precipitation. To maintain the
499   equilibrium of the system, hydroxide ions released from portlandite dissolution diffuse
500   towards the external solution, causing mass reduction. Measures of pH at the end of the
501   test confirm higher leaching rates in the mortars submerged in the Na_2SO_4 solution
502   compared to control (9.46 and 8.73, respectively), while calcium content by ICP-OES at
503   the end of the test also indicates that calcium leaching phenomenon is more pronounced
504   in the aggressive solutions (88.37 ppm over 56.06 ppm). These phenomena should be
505   intensified as porosity and permeability of the specimen increases, in line with the
506   initial trends depicted in Figure 8.
507
508   The slope reduction shown by non-air-entrained mortars at later stages of the attack
509   indicates a deceleration of the leaching process, which could be explained by lower
510   concentration gradients between external and internal solutions and the pore-filling
511   effect caused by the precipitation of phases in the superficial pores of the specimens. As
512   described in Figure 4, non-air-entrained mortars present a thin dense external layer that
513   might slow down the leaching process. On the other hand, this dense layer is not visible
514   in AE0.45_18.8% series, which could explain why in this composition the leaching
515   phenomenon seems to progress at a similar rate until the end of the test. The particularly
516   high mass gain experienced by 0.55_13.7% from 200 days on could be explained by a
517   macroscopic swelling caused by the large expansions measured. Notice that this age
518   corresponds to the age when the expansion of this series becomes the highest amongst
519   all compositions studied (see Figure 5).
520
521   The physical changes observed here suggest that the role of the pore network during
522   ESA is not only related to the transport process and the amount of expansive phases
523   formed. According to the results obtained, the buffer capacity of the matrix to

524 accommodate the product precipitated might be more relevant than the permeability
525 itself when it comes to define the durability of the specimens at early stages of the
526 attack.
527
528 3.2 MICRO-STRUCTURAL ANALYSIS
529
530 3.2.1 XRD ANALYSIS
531
532 This section presents the evolution of phase composition measured by quantitative XRD
533 analysis for the different compositions during sulphate exposure. To simplify the
534 interpretation of the results, only crystalline phases interacting with the sulphate ions are
535 presented and phase contents are expressed as a percentage of the cement content.
536
537 Figure 9 depicts ettringite, gypsum and portlandite contents for all compositions at the
538 end of the test. The sum of expansive phases (ettringite and gypsum) range between
539 14.3 % in the composition with 0.38 water/cement ratio and 29.9 % in the air-entrained
540 mortars. On the other hand, Portlandite contents only present a slight variation, with
541 values between 14.0 % and 17.6 % for 0.38_8.1% and AE0.45_18.8%, respectively. As
542 expected, Rietveld quantification reveals increasing amounts of expansive phases with
543 the increase of porosity of the composition, with results suggesting that the pore system
544 affects the sulphate penetration rate of each composition, causing precipitation of
545 different amounts of expansive products.
546
547 Figure 9 also includes the radial expansions measured at 365 days with its
548 corresponding +1/-1 standard deviation bars. Results indicate no clear relationship
549 between the amounts of expansive phases and the final radial expansions measured.
550 Although the amount of expansive phases in AE0.45_18.8% is 2.1 times bigger than in
551 0.38_8.1%, the final radial free expansion obtained decreases by a factor of 5.7.
552
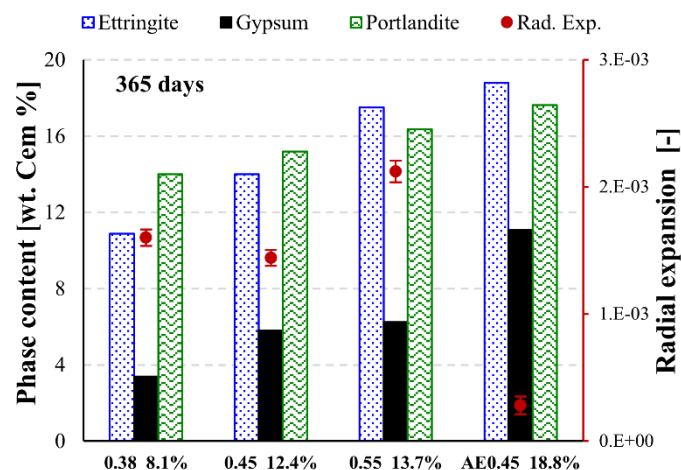
553
554
555 In order to further evaluate the relationship between expansive phases and expansions at
556 different stages of the attack, Figure 10 shows the evolution of ettringite, gypsum and
557 portlandite contents combined with the radial expansions for 0.45_12.4% and
558 AE0.45_18.8% mortars at 28, 90, 180, 270 and 365. These compositions were selected
559 for presenting the same water/cement ratio and aggregate content, with the main
560 difference the presence of air voids intruded by the air-entraining agent. Both

561 compositions already show high ettringite and gypsum contents after 28 days of
562 exposure.
563
564 After that, 0.45_12.4% depicts similar contents until the end of the test (-0.1 % between
565 28 and 365 days) while AE0.45_18.8% shows a moderate increase (+8.9 % between 28
566 and 365 days). In both cases, the increments of expansion and the amount of expansive
567 phases formed during the same period do not seem to present any direct relationship at
568 any stage of the attack. Series 0.45_12.4% clearly illustrates this statement. Even
569 though expansion increases by $9.8 \cdot 10^{-4}$ between 28 and 365 days, the amount of
570 expansive phases remain almost unaltered. Again, this suggests that the progressive
571 precipitation of expansive phases consumes part of the buffering capacity of the pore
572 system. Once the buffering capacity is reduced, precipitations of even small amounts of
573 expansive phases lead to significant expansion.
574
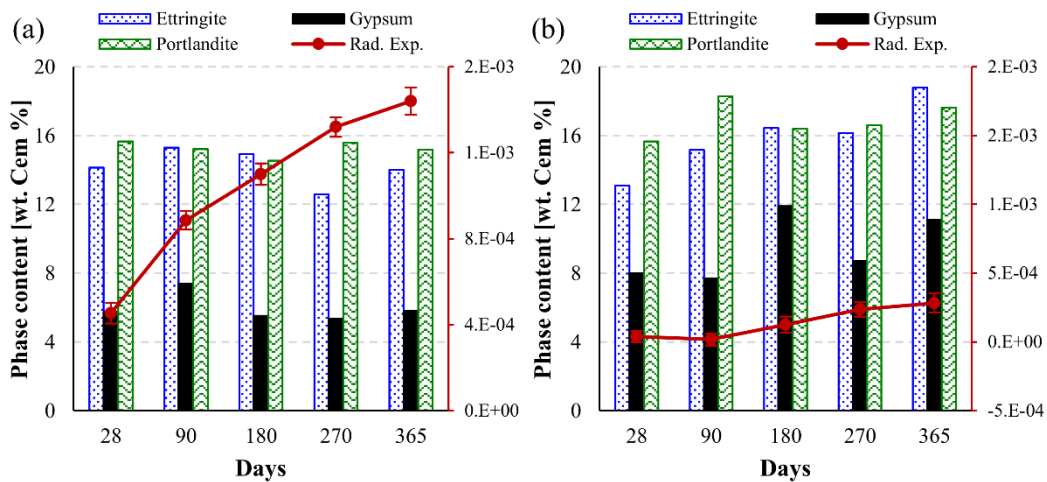
575
576
577 ESA-related expansions have traditionally been attributed to the additional volume
578 generated by ettringite formation. Therefore, dimensional variations should imply the
579 precipitation of expansive phases. However, the results obtained depicts no clear link
580 between these two variables. This is in agreement with other studies of the literature
581 [34,35] that did not find any clear correlation between the amount of ettringite formed
582 and the expansions observed. Amongst the other possible ESA expansion mechanisms
583 that have been suggested in the literature [2], the crystallisation pressure theory might
584 be the only one that could explain the results obtained.
585
586 This theory states that expansions are originated from the crystallisation pressure
587 developed by ettringite formation in a supersaturated pore solution [4,5,36]. According
588 to this theory, only ettringite formed in small pores is likely to generate enough pressure
589 to cause damage [34]. During the initial stages of exposure, there is rapid increase of
590 sulphate content in the pore network causing the early precipitation of expansive phases.
591 Due to the extremely high concentration of sulphates and the inability to generate
592 enough ettringite to reduce the degree of supersaturation in regions with a very refined
593 matrix, there is a crystallisation pressure boost at these locations. This pressure is
594 responsible for the degradation and damage observed during the first stage of the attack
595 (Figures 5 and 7). At later stages, due to a lower penetration rate caused by the pore-
596 filling effect, this excess of sulphate ions can be allocated to other locations, more
597 thermodynamically stable, with a consequent decrease in crystallisation pressure. This

598 phenomenon is reflected on the macro-scale by a reduction of the expansions and
599 degradation rates, as observed in Figures 5 and 7.
600
601 In the case of AE0.45_18.8%, the absence of expansions during the initial stage might
602 be explained by the large availability of locations to accommodate the initial ettringite
603 precipitated and sulphate excess without developing high crystallisation pressures.
604 Unlike more refined matrices, the air-entrained mortars do not experience a significant
605 reduction of sulphate penetration due to the pore-filling effect (Figure 1). Consequently,
606 sulphate content continues to increase at a steady rate until crystallisation pressure starts
607 to develop in some parts of the matrix. This phenomenon might explain the slight
608 expansion and degradation observed after 150 days of exposure (Figures 5 and 7).
609
610 3.2.2 CHARACTERISATION OF THE PORE STRUCTURE
611
612 This section presents the results of a comprehensive analysis of the pore size
613 distribution performed by MIP tests at 14, 28, 90, 180 and 270 days to obtain a
614 qualitative picture of the evolution of the pore network throughout the attack. Figure 11
615 shows the evolution of the total volume of mercury intruded and MIP porosity for all
616 mortars under sulphate exposure. The error bars included correspond to +1/-1 standard
617 deviation. As expected, the volume intruded and porosity increases with increasing
618 water/cement ratio and addition of an air-entrainer. Initial porosities at 14 days ranged
619 between 8.1 % and 13.7 % for mortars with a water/cement ratio between 0.38 and 0.55.
620 In air-entrained mortars, porosities of 18.8 % were observed due to the inclusion of air
621 bubbles.
622
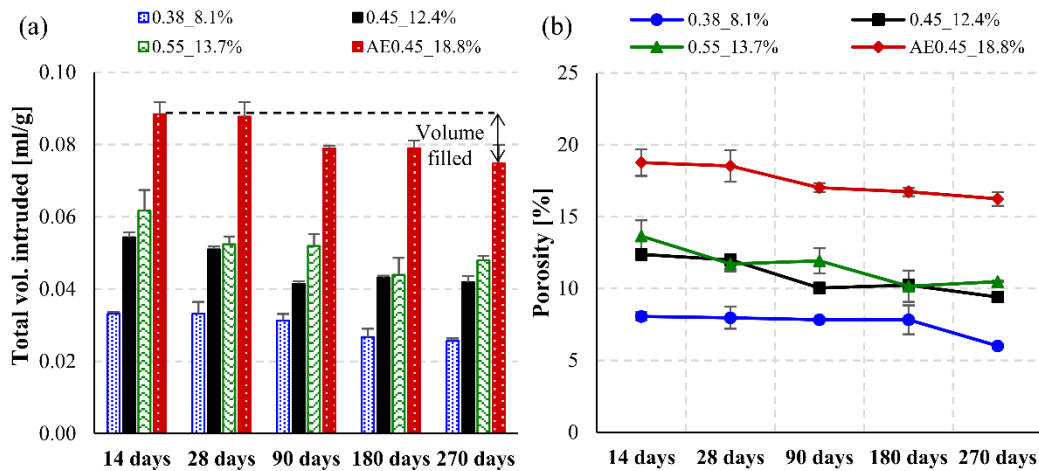
623
624
625 As the attack proceeds, the mercury intruded and porosity decrease as a result of normal
626 cement hydration processes and the precipitation of expansive phases in the pore
627 network. The difference between the total volume intruded at 14 and 270 days allows
628 the assessment of the pore volume filled by these two phenomena in each composition.
629 Mortars with higher porosity (0.55_13.7% or AE0.45_18.8%) display 1.8 times more
630 pore volume filled than the composition 0.38_8.1%. This result suggests that both
631 cement hydration and precipitation of expansive phases are more significant in
632 compositions with higher porosities, in line with the XRD results shown in Figure 9.
633
634 However, the assessment of the fraction of volume filled from the initial total pore
635 volume depicts different trends. In this case, 0.38_8.1% mortars show 1.5 times more

636   ratio of volume filled than AE0.45_18.8% between 14 and 270 days. This result
637   suggests that despite mortars with refined pore networks present lower precipitation of
638   expansive phases and slower cement hydration, the volume filled represents a higher
639   fraction of the total volume available. Therefore, in these compositions the pore-filling
640   effect is more significant. These trends correspond to the visual inspection of the
641   specimens described in section 3.1.1.
642
643   Figure 12 shows the evolution of the critical pore diameter for 0.38_8.1%, 0.45_12.4%
644   and 0.55_13.7% under sulphate exposure at 14, 28, 90, 180 and 270 days, with the error
645   bars included corresponding to +1 standard deviation. This semi-quantitative parameter
646   can be usually related to the permeability of the material [20]. Results for
647   AE0.45_18.8% series are not included as the air bubbles produce high increments of
648   intrusion in large diameters which distort the assessment and hinder comparison with
649   the other compositions.
650
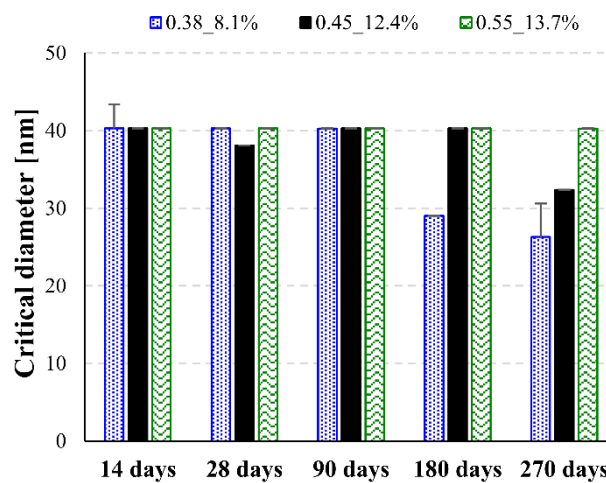
651
652
653   Despite the differences in porosity, non-air-entrained mortars present similar critical
654   diameters until 90 days of exposure. After that, mortars with low water/cement ratios
655   display an important reduction of critical diameter, with this trend becoming even more
656   evident at the end of the evaluated period. The inability of the critical diameter to
657   capture differences in the permeability during the early stages of the attack might be
658   explained by the fact that this parameter does not account for the most accessible path
659   for fluid transport in the cement paste but the mean pore size that allows maximum
660   percolation. Results suggest that these pores might only be affected at late stages of the
661   attack, when the most accessible paths are reduced due to the pore-filling effect and the
662   formation of the thin layer described in section 3.1.1.
663
664   Figure 13 shows the evolution of the pore size distribution of all mortars according to 5
665   predefined pore ranges (<10 nm, 10-50 nm, 50-100 nm, 100-500 nm and >500 nm). The
666   error bars included correspond to +1/-1 standard deviation. This figure shows how
667   sulphate exposure alters the pore-size distribution of the material and allows a
668   qualitative assessment of the precipitation patterns amongst the different compositions.
669   The evolution of the different pore ranges between 14 and 270 days shows similar
670   trends for the non-air-entrained mortars. For these compositions, the refinement of the
671   pore network during the attack is mainly caused by the reduction of pores between 50 –
672   100 nm. This pore range accumulates the 63.0 %, 66.4 % and 58.2 % of the total

673 volume filled by the combined action of cement hydration and precipitation of
674 expansive phases in 0.38_8.1%, 0.45_12.4% and 0.55_13.7%, respectively. However,
675 the AE0.45_18.8% series only accumulates 31.1 % of the volume filled in this pore
676 range. In this case, the main reduction of intrusion is observed in pores of 100 - 500 nm,
677 which concentrates the 60.4 % of the reduction.
678
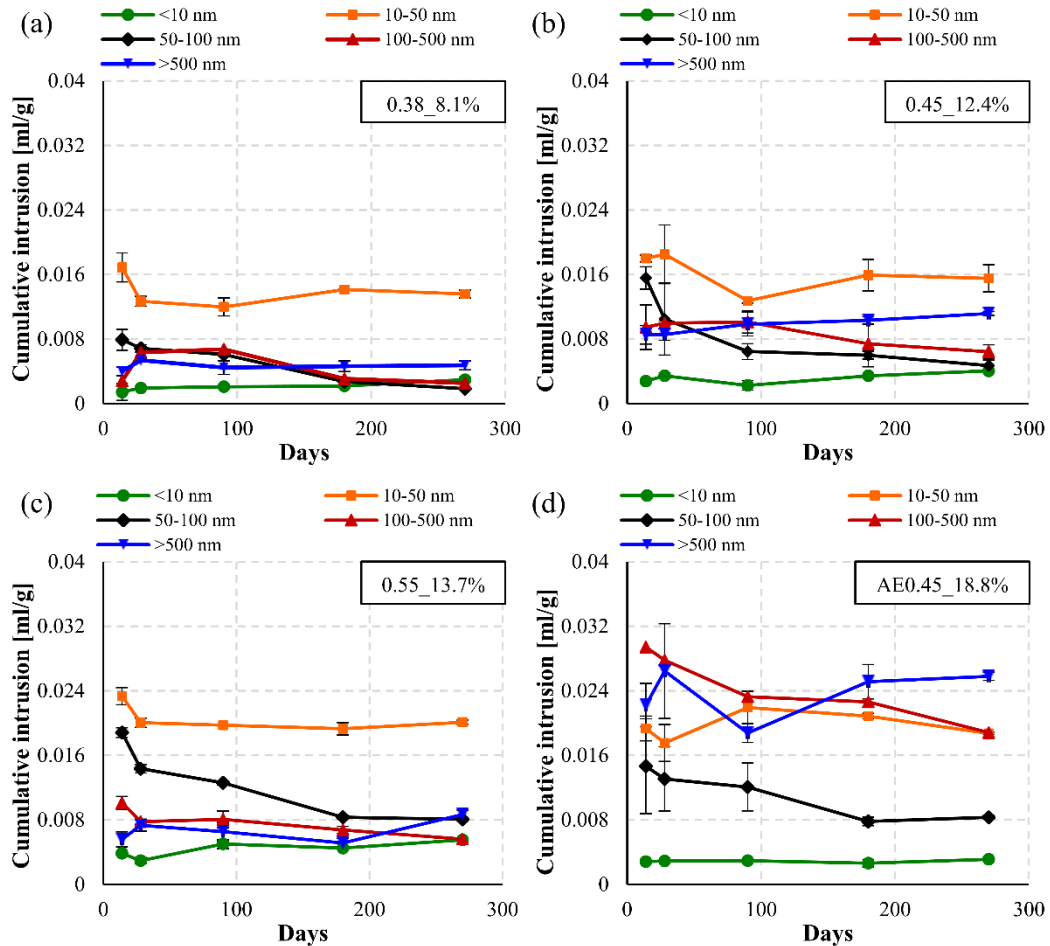
679
680
681 Although the pore sizes measured in the MIP technique do not necessarily match the
682 real pore size distribution of the material, the qualitative analysis of the results highlight
683 that the pore sizes affected during ESA vary depending on the characteristics of the pore
684 system of the matrix. Results indicate that in air-entrained mortars, the alterations in the
685 pore network are produced in bigger pore ranges than the observed in other
686 compositions, which is in agreement with other studies [37]. The bigger pores of
687 AE0.45_18.8 act as pressure releases that limit the pressure increase in the system,
688 especially in smaller pores. This pressure release effect combined with the capacity to
689 accommodate expansive phases might explain the lower degrees of damage observed in
690 AE0.45_18.8.
691
692 **4. CONCEPTUAL MODEL OF THE ROLE OF POROSITY**
693
694 The approach adopted in the codes to obtain durable materials against ESA is based on
695 a fairly simple perception of the role of the porosity. It assumes that the amount of
696 ettringite precipitated defines the damage generated in the material. Therefore, codes
697 prescribe materials with low permeability to reduce the penetration of sulphate ions.

698   However, this study shows that the amount of expansive phases itself is not always a
699   good indicator of the level of deterioration. Sometimes, other aspects such as the
700   location of the precipitation and the presence of pressure release pores might play a
701   more significant role in the outcome of the attack.

702

703   The results obtained in this study highlight two mechanisms defined by the pore
704   network that contribute to ESA resistance: permeability, which is related to the amount
705   of expansive phases potentially generated, and buffer capacity, which might define the
706   preferential location of the precipitation of expansive products. Overall ESA resistance
707   defined by the pore network is the result of the contribution of these two mechanisms.
708   Since the pore network characteristics do not remain constant over time (due to cement
709   hydration and pore-filling effect), the contribution of these two mechanisms also varies
710   during the attack.

711

712   Figure 14 represents this phenomenon in a schematic way. A material with low porosity
713   achieves high durability by the low permeability of the matrix, which hinders sulphate
714   ingress and potential ettringite precipitation. As porosity increases, sulphate penetration
715   is promoted, thus reducing the durability of the material. The buffer capacity curve,
716   however, shows an opposite trend. In this case, ESA resistance increases for high values
717   of porosity due to a preferential precipitation in large pores and decreases along the
718   refinement of the pore network. Notice that this model does not account for the effects
719   of crack formation. The model depicted in Figure 14 therefore represents the role of
720   porosity during the attack prior to the onset of cracking.

721
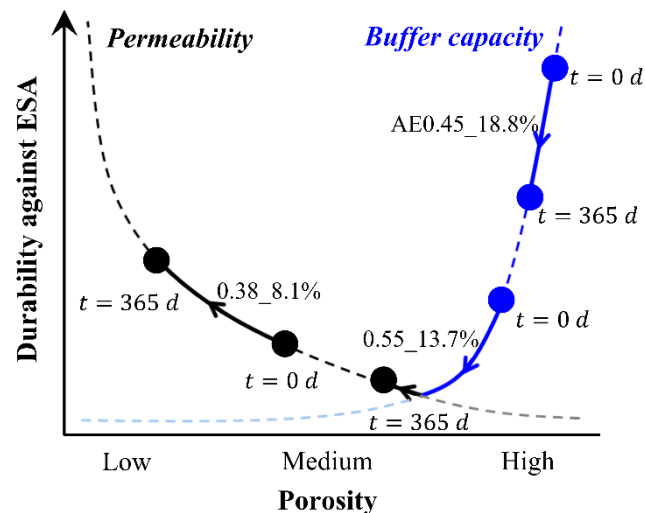
722

723

724   Figure 14 includes a qualitative location of 0.38_8.1%, 0.55_13.7% and AE0.45_18.8%
725   based on the porosity of these compositions. 0.45_12.4% is not depicted for clarity in
726   the interpretation of the graph. At early stages of the attack, 0.38_8.1% presents the
727   lowest durability, which is reflected by displaying the largest expansions amongst the
728   compositions evaluated (Figure 5). As time proceeds, the durability of this composition
729   improves due to a reduction of porosity, which results in a decrease of the expansion
730   rate.

731

732   Meanwhile, the air-entrained mortar initially presents the highest durability due to the
733   large buffer capacity of the matrix (no expansions measured). Despite durability reduces
734   over time as the precipitation of expansive phases reduce the buffer capacity, this

composition keeps displaying the highest potential durability against ESA at the conclusion of the test. Finally, 0.55_13.7% mortars display a half-way behaviour with an initial stage characterised by a pore system that is capable of accommodating part of the expansive phases. A decrease in durability is caused by the precipitation of expansive phases that reduces the buffer effect of the porosity.

Further research on the use of air-entrainers with other mortar mixtures is recommended to validate the buffer capacity curve shown in Figure 14. The design of durable materials against ESA based on high buffer capacities should be made with caution. In these cases, durability tends to drop off over time as the pore-filling effect has a negative impact on the matrix buffer capacity, while the continuous formation of ettringite might lead to a significant strength-loss of the material due to decalcification of portlandite or C-S-H gel. The approach based on low permeability is safer however, as the pore-filling effect developed over time has a positive impact on permeability.

5. CONCLUSIONS

The following specific findings may be derived from this study.

- Expansion measurements suggest that the buffer capacity of the pore structure defines the damage developed during the early stages of ESA. After that, the transport process affected by the precipitation of expansive phases controls the durability. The duration of the first stage can be extended if sufficient number of large pores relative to the amount of ettringite formed are available in the material.

- Air-entrained mortars displayed the lowest expansion and ultrasonic-pulse velocity variation over time, possibly characterised by the smallest damage level amongst all compositions tested. MIP results suggest that this behaviour might be explained by a preferential precipitation of expansive phases in large pores, which buffers the pressure increase in the pore system and accommodates expansive phases without causing damage.

- Quantitative XRD analyses shows no direct relationship between the damage generated and the amount of expansive product formed during any stage of the attack. In fact, the biggest precipitation of expansive phases was found in the composition that presents the least expansion.

REFERENCES

[1]   M. Alexander, A. Bertron, N. De Belie, Performance of Cement-Based Materials in Aggressive Aqueous Environments, Springer, 2013.

784   [2]   J.P. Skalny, I. Odler, J. Marchand, Sulfate Attack on Concrete, Spon, London,
785   2001.
786   [3]   R. Tixier, B. Mobasher, Modeling of Damage in Cement-Based Materials
787   Subjected to External Sulfate Attack. I: Formulation, J. Mater. Civ. Eng. 15 (2003) 305–
788   313.
789   [4]   G.W. Scherer, Stress from crystallization of salt, Cem. Concr. Res. 34 (2004)
790   1613-1624.
791   [5]   R.J. Flatt, G.W. Scherer, Thermodynamics of crystallization stresses in DEF,
792   Cem. Concr. Res. 38 (2008) 325-336.
793   [6]   C. Yu, W. Sun, K. Scrivener, Mechanism of expansion of mortars immersed in
794   sodium sulphate solutions, Cem. Concr. Res. 43 (2013) 105-111.
795   [7]   F.P. Glasser, J. Marchand, E. Samson, Durability of concrete — Degradation
796   phenomena involving detrimental chemical reactions, Cem. Concr. Res. 38 (2008) 226-
797   246.
798   [8]   A. Çavdar, S. Yetgin, Investigation of mechanical and mineralogical properties
799   of mortars subjected to sulphate, Constr. Build. Mater. 24 (2010) 2231-2242.
800   [9]   R. El-Hachem, E. Rozière, F. Grondin, A. Loukili, Multi-criteria analysis of the
801   mechanism of degradation of Portland cement based mortars exposed to external
802   sulphate attack, Cem. Concr. Res. 42 (2012) 1327-1335.
803   [10]   W. Piasta, J. Marczewska, M. Jaworska, Durability of air entrained cement
804   mortars under combined sulphate and freeze-thaw attack, Procedia Eng. 108 (2015) 55-
805   62.
806   [11]   T. Ikumi, S.H.P. Cavalaro, I. Segura, A. de la Fuente, A. Aguado, Simplified
807   methodology to evaluate the external sulphate attack in concrete structures, Mater. Des.
808   89 (2016) 1147-1160.
809   [12]   I. Oliveira, S.H.P. Cavalaro, A. Aguado, New kinetic model to quantify the
810   internal sulphate attack in concrete, Cem. Concr. Res. 43 (2013) 95–104.
811   [13]   T. Ikumi, S.H.P. Cavalaro, I. Segura, A. Aguado, Alternative methodology to
812   consider damage and expansions in external sulphate attack modeling, Cem. Concr.
813   Res. 63 (2014) 105-116.
814   [14]   N.N. Naik, A.C. Jupe, S.R. Stock, A.P. Wilkinson, P.L. Lee, K.E. Kurtis, Sulfate
815   attack monitored by microCT and EDXRD: Influence of cement type, water-to-cement
816   ratio, and aggregate, Cem. Concr. Res. 36 (2006) 144-159.
817   [15]   M. Santhanam, M.D. Cohen, J. Olek, Mechanism of sulphate attack: A fresh
818   look Part 1: Summary of experimental results, Cem. Concr. Res. 32 (2002) 915-921.
819   [16]   M. Santhanam, M.D. Cohen, J. Olek, Mechanism of sulphate attack: a fresh look
820   Part 2. Proposed mechanisms, Cem. Concr. Res. 33 (2003) 341-346.
821   [17]   A.E. Idiart, C.M. López, I. Carol, Chemo-mechanical analysis of concrete
822   cracking and degradation due to external sulphate attack: A meso-scale model, Cem.
823   Concr. Compos. 33 (2011) 411-423.
824   [18]   R. El-Hachem, E. Rozière, F. Grondin, A. Loukili, New procedure to investigate
825   external sulphate attack on cementitious materials, Cem. Concr. Compos. 34 (2012)
826   357-364.
827   [19]   A. Chabrelie, Mechanisms of degradation of concrete by external sulphate ions
828   under laboratory and field conditions, PhD Thesis, ÉPFL, Lausanne, 2010.
829   [20]   I. Segura, Caracterización del proceso de descalcificación en morteros, mediante
830   ensayos destructivos y no destructivos, PhD Thesis, ETSICCP, Madrid, 2008.
831   [21]   D. Jansen, F. Goetz-Neunhoeffer, C. Stabler, J. Neubauer, A remastered external
832   standard method applied to the quantification of early OPC hydration, Cem. Concr. Res.
833   41 (2011) 602-608.

834 [22]   D. Jansen, C. Stabler, F. Goetz-Neunhoeffer, S. Dittrich, J. Neubauer, Does
835 Ordinary Portland Cement contain amorphous phase? A quantitative study using an
836 external standard method, Powder Diffract. 26 (2011) 31-38.
837 [23]   R. Snellings, A. Bazzoni, K. Scrivener, The existence of amorphous phase in
838 Portland cements: Physical factors affecting Rietveld quantitative phase analysis, Cem.
839 Concr. Res. 59 (2014) 139-146.
840 [24]   A.G. de la Torre, S. Bruque, J. Campo, M.A.G. Aranda, The superstructure of
841 C3S from synchrotron and neutron powder diffraction and its role in quantitative
842 analysis, Cem. Conc. Res. 32 (2002) 1347-1356.
843 [25]   W.G. Mumme, R.J. Hill, G.W. Bushnell, E.R. Segnite, Rietveld crystal structure
844 refinements, crystal chemistry and calculated powder diffraction data for the
845 polymorphs of dicalcium silicate and related phases, N. Jb. Miner. Abh. (J. Min.
846 Geochem.) 169 (1995) 35-68.
847 [26]   H.E. Petch, The hydrogen positions in portlandite, Ca(OH)2, as indicated by the
848 electron distribution, Acta Crystallogr. 14 (1961) 950-957.
849 [27]   R. Wartchow, Datensammlung nach der ''learnt profile''-methode(LP) für calcit
850 und vergleich mit der ''background peak background''-methode (BPB), Z. Kristallogr.
851 186 (1989) 300-302.
852 [28]   F. Goetz-Neunhoeffer, J. Neubauer, Refined ettringite structure for quantitative
853 X-ray diffraction analysis, Powder Diffr. 21 (2006) 4-11.
854 [29]   W.A. Wooster, On the crystal structure of gypsum CaSO4(H2O)2, Z.
855 Kristallogr. 94 (1936) 375-396.
856 [30]   A.A. Colville, S. Geller, The crystal structure of brownmillerite, Ca2FeAlO5,
857 Acta Crystallogr. B 27 (1971) 2311-2315.
858 [31]   L. Levien, C.T. Prewitt, D.J. Weidner, Structure and elastic properties of quarz
859 at pressure, Am. Mineral. 65 (1980) 920-930.
860 [32]   E.N. Maslen, V.A. Streltsov, N.R. Streltsova, N. Ishizawa, Y. Satow,
861 Synchrotron X-ray study of the electron density in alpha-Al2O3, Acta Crystallogr. B 49
862 (1993) 973-980.
863 [33]   E. Sakai, T. Kasuga, T. Sugiyama, K. Asaga, M. Daimon, Influence of
864 superplasticizers on the hydration of cement and the pore structure of hardened cement,
865 Cem. Concr. Res. 36 (2006) 2049-2053.
866 [34]   W. Müllauer, R.E. Beddoe, D. Heinz, Sulfate attack expansion mechanisms,
867 Cem. Concr. Res. 52 (2013) 208-215.
868 [35]   W. Kunther, B. Lothenbach, K. Scrivener, On the relevance of volume increase
869 for the length changes of mortar bars in sulphate solutions, Cem. Concr. Res. 46 (2013)
870 23-29.
871 [36]   C. Yu, W. Sun, K. Scrivener, Degradation mechanism of slag blended mortars
872 immersed in sodium sulphate solution, Cem. Concr. Res. 72 (2015) 37-47.
873 [37]   T. Ikumi, I. Segura, S.H.P. Cavalaro, Influence of early sulphate exposure on the
874 pore network development of mortars, Constr. Build. Mater. 143 (2017) 33-47.